



Polystyrene spheres-templated mesoporous carbonous frameworks implanted with cobalt nanoparticles for highly efficient electrochemical nitrate reduction to ammonia

Suxian Xu^a, Yongbin Shi^a, Zhibing Wen^a, Xiao Liu^a, Yong Zhu^a, Guoquan Liu^a, Hua Gao^a, Licheng Sun^{a,b,c}, Fei Li^{a,*}

^a State Key Laboratory of Fine Chemicals, DUT-KTH Joint Education and Research Centre on Molecular Devices, Dalian University of Technology, Dalian 116024, China

^b Center of Artificial Photosynthesis for Solar Fuels, School of Science, Westlake University, Hangzhou 310024, China

^c Department of Chemistry, School of Engineering Sciences in Chemistry, Biotechnology and Health, KTH Royal Institute of Technology, Stockholm 10044, Sweden

ARTICLE INFO

Keywords:

Nitrate reduction reaction
Hierarchically porous carbon skeleton
Co nanoparticles
Heterogeneous electrocatalysis
in-situ Raman

ABSTRACT

Electrocatalytic nitrate reduction reaction (eNO₃RR) to ammonia (NH₃) provides an intriguing approach for both environmental denitrification and sustainable NH₃ synthesis. Herein, we report the fabrication of hierarchically mesoporous Co nanoparticles decorated N-doped carbon composites as a highly efficient electrocatalyst for eNO₃RR by using monodispersed polystyrene spheres (PS) as sacrificial templates (MR Co-NC). By taking advantage of the large specific area of the pore-rich structures and the high intrinsic activity of metallic Co, the MR Co-NC shows remarkable activity toward eNO₃RR, which achieves a partial current density of 268 mA cm⁻² with a Faradaic efficiency (FE) of 95.35 ± 1.75 % and a generation rate of 1.25 ± 0.023 mmol h⁻¹ cm⁻² for NH₃ production under the optimal conditions. The porous carbon skeleton was found to play a dual role by simultaneously protecting the active sites from oxidation and facilitating long-range charge and mass transfer. Theoretical calculations reveal a lower energy barrier of the rate-determining step (*NO₂ + H₂O + 2e⁻ → *NO + 2OH⁻) on the metallic Co of MR Co-NC over β-Co(OH)₂ formed by the reconstruction of carbon-free Co nanoparticles.

1. Introduction

Ammonia (NH₃) holds a high status for food production as it is the main component of fertilizer. It has also been recognized as both a promising green liquid fuel as well as an easily transportable carbon-free hydrogen-rich (17.6%wt H₂) energy carrier [1,2]. The traditional Haber-Bosch (H-B) process for NH₃ synthesis is energy-intensive, which operates under high pressure (150–250 atm) and high temperature (350–550 °C) [3,4]. As a promising alternative to the traditional H-B process, electrocatalytic nitrogen reduction reaction (eNRR) has attracted intense interest owing to its merits of energy-saving and environmentally benign in NH₃ synthesis [5,6]. Despite the potentiality, the difficulty of breaking the strong N≡N triple bond (941 kJ mol⁻¹) associated with high reaction energy barriers and limited N₂ solubility in aqueous media often result in poor Faradaic efficiency and ultra-low NH₃ yield rates, making this method farfetched for mass production up to now [7–9].

Another alternative for NH₃ production is the electrocatalytic reduction of nitrate (NO₃) [10]. Compared to the electrocatalytic nitrogen reduction reaction using gaseous N₂ with extremely low solubility in aqueous solutions, the electro-reduction of water-soluble nitrate is more favorable and promising. Nitrate is a known toxic contaminant, ubiquitously exists in the environment due to excessive crop fertilization and industrial activity. Therefore, conversion of nitrate released by human beings contributes to restoring the global nitrogen cycle [11]. Under alkaline conditions, nitrate reduction with a thermodynamic potential (0.69 V vs. RHE) is considered more favorable than N₂ reduction [12]. Thus, from both environmental and economic points of view, electrocatalytic NO₃ reduction reaction (eNO₃RR) to NH₃ represents significant opportunities for sustainable NH₃ economy. In the literature, some efficient electrocatalysts such as Au₁Cu (111), single-atom alloys [13], single-atom Fe catalyst [14], and Cu/Pd/CuO_x [15] have been exploited for eNO₃RR. However, it is still a challenge to simultaneously yield high NH₃ Faradaic efficiency (FE) (> 90%) and

* Corresponding author.

E-mail address: lifei@dlut.edu.cn (F. Li).

<https://doi.org/10.1016/j.apcatb.2022.122192>

Received 18 September 2022; Received in revised form 1 November 2022; Accepted 15 November 2022

Available online 21 November 2022

0926-3373/© 2022 Elsevier B.V. All rights reserved.

high partial current density ($> 200 \text{ mA cm}^{-2}$) under ambient conditions due to the parasitic side reactions.

Transition metal-hybridized nitrogen-doped carbon materials (M-NC) have drawn great attention as promising heterogeneous catalysts owing to their durable stability and tunable composition [16,17], M-NC catalysts were typically fabricated by the annealing of molecular precursors or MOFs-based materials, which possess micro- or mesopores with pore sizes lower than 5 nm, limiting the accessibility of active metal sites. Especially when a high metal loading was applied, some active sites are buried by the carbon matrix and in poor contact with the electrolytes [18]. To alleviate this drawback, three-dimensional (3D) structures with sufficient spacious pores and interconnected channels have shown advantages in maximizing the exposure of active sites and enabling a continuous electronic transmission and multiple pathways for electrolyte diffusion. Given the merits of tunable size and easy removal, polystyrene spheres (PS) have been employed as sacrificial templates for M-NC fabrication and the resulting highly porous M-NC materials have achieved high performance in photocatalytic CO_2 reduction reaction [19], aluminum-ion batteries [20], and hydrogenation of biomass [21]. However, PS-templated M-NC has never been applied for eNO_3RR .

Herein, we report a facile strategy for the fabrication of a Co-based nitrogen-doped carbon catalyst with a 3D mesopore-rich structure (denoted as MR Co-NC) by employing PS as sacrificial templates. The unique 3D mesoporous carbon framework was found to not only accelerate electron and mass transportation, but also improve the catalytic activity by exposing more active sites. Moreover, in-situ Raman spectroscopy complemented with *ex-situ* XRD diffraction tests revealed the role of the carbon skeleton in preventing the active metal sites from reconstruction in alkaline solution. With the MR Co-NC as the electrocatalyst for eNO_3RR , a high Faradaic efficiency (FE) of $95.35 \pm 1.75\%$ and an excellent NH_3 yield rate up to $1.25 \pm 0.023 \text{ mmol h}^{-1} \text{ cm}^{-2}$ were obtained, which outperform the reported state-of-the-art eNO_3RR catalysts.

2. Experimental procedures

2.1. Chemicals

Cobaltous nitrate hexahydrate, 2-methylimidazole, zinc nitrate hexahydrate, 1,10-phenanthroline, 5% ammonium ferric sulfate solution, maleic acid, styrene, potassium persulfate, sodium laurylsulfonate, sodium citrate dihydrate, salicylic acid, potassium hydroxide, potassium nitrate- ^{15}N (K^{15}NO_3 , 99 atom%; $\geq 98.5\%$), ammonium chloride- ^{15}N (99 atom %), hydrazine standard solution (analytical standard, $1000 \mu\text{g mL}^{-1}$ in $1.0 \text{ mol L}^{-1} \text{ HCl}$), sodium nitroprusside dihydrate, p-dimethylaminobenzaldehyde, N-(1-naphthyl) ethylenediamine dihydrochloride, sulfanilamide and sodium hydroxide were purchased from Macklin chemical company and without any further purification. Ethanol, hydrochloric acid and sodium hypochlorite solution ($\text{pCl} \geq 10.0\%$) were analytical pure and obtained from commercial supplier. Ar gas (99.999%) was purchased from DALIAN GUANGMING SPECIAL GAS CO., LTD. The carbon paper (CP) was purchased from TORAY Industries, Japan. Millipore water (resistivity: ca. $18.2 \text{ M}\Omega \text{ cm}$) was applied to prepare the electrolyte solution.

2.2. Catalysts preparation

2.2.1. Synthesis of polystyrene spheres (PS)

Monodispersed polystyrene spheres with diameters of 70–80 nm were synthesized by emulsion polymerization. [20] Typically, sodium laurylsulfonate (emulsifying agent, 0.4 g) was dissolved in 360 mL of deionized H_2O with a three-necked round-bottom flask (500 mL) followed by the addition of 40 mL of styrene. After adding 0.54 g of potassium persulfate, the reaction was performed at 70°C for 5 h under an Ar atmosphere. The obtained suspension was centrifuged at 4000 rpm to

remove any large agglomerates at the bottom and the upper suspension was dried at 60°C overnight to obtain the PS spheres with a diameter of 70–80 nm.

2.2.2. Synthesis of MR Co-NC

In a typical synthetic process, a methanolic solution containing $\text{Co}(\text{NO}_3)_2 \cdot 6 \text{H}_2\text{O}$ (0.02 g mL^{-1}) was prepared as a precursor solution. The as-prepared PS spheres (2.5 g) were added into the precursor solution and stood for 1 h. The resulting mixture was further treated with vacuum degassing for 30 min to ensure that all template voids were filled with precursor solution. The impregnated composite was transferred to a beaker and dried at 50°C overnight to obtain a pink powder. The powder was then poured into a solution of 2.5 g of 2-methylimidazole and 100 mL of methanol and stirred at room temperature for 24 h to obtain a purple product, which was denoted as ZIF-67 @PS. The MR Co-NC was synthesized by pyrolyzing the ZIF-67 @PS at 600°C for 3 h in an Ar atmosphere with a heating rate of 2°C min^{-1} .

2.2.3. Synthesis of Co-NC

The Co-NC was synthesized by using conventional ZIF-67 as the MOF template without the PS sphere. Typically, 2.0 g of $\text{Co}(\text{NO}_3)_2 \cdot 6 \text{H}_2\text{O}$ was dissolved in 100 mL of methanol with stirring. Then 100 mL of methanol containing 2.5 g of 2-methylimidazole was added followed by vigorous stirring for 24 h at room temperature under atmospheric pressure. The obtained ZIF-67 was separated by centrifugation, washed with methanol for several times, and finally dried at 60°C under vacuum overnight. The final Co-NC was obtained by pyrolysis at 600°C for 3 h in an Ar atmosphere with a heating rate of 2°C min^{-1} .

2.2.4. Synthesis of NC

The ZIF-8 @PS was prepared following the same procedure as ZIF-67 @PS except that the $\text{Co}(\text{NO}_3)_2 \cdot 6 \text{H}_2\text{O}$ was replaced by $\text{Zn}(\text{NO}_3)_2 \cdot 6 \text{H}_2\text{O}$. The NC was synthesized by pyrolyzing the ZIF-67 @PS at 900°C for 3 h in an Ar atmosphere with a heating rate of 5°C min^{-1} .

2.2.5. Synthesis of Co NPs

1.0 g of $\text{Co}(\text{CH}_3\text{COO})_2 \cdot 4 \text{H}_2\text{O}$ was added to 7.5 mL of ethanol. A white slurry prepared by mixing 2.5 g of NaOH with 5.0 mL of 50% $\text{N}_2\text{H}_4 \cdot \text{H}_2\text{O}$ solution was added to the above solution under magnetic stirring. The produced precipitate was washed with aqua-ammonia to remove the by-product, followed by rinsing with ethanol and water several times and freeze-drying overnight. The Co NPs were then obtained by annealing at 300°C in a 5% H_2/Ar atmosphere for 2 h.

2.2.6. Synthesis of $\beta\text{-Co}(\text{OH})_2$

$\beta\text{-Co}(\text{OH})_2$ was synthesized by a hydrothermal method. Initially, two solutions were prepared by dissolving 0.9 M $\text{Co}(\text{NO}_3)_2 \cdot 6 \text{H}_2\text{O}$ in 30 mL of ultra-pure water and 0.8 M Na_2CO_3 and 1.92 M NaOH in 30 mL of ultra-pure water through ultrasonication for 10 min. The two solutions were mixed by vigorous stirring and a 60 mL of the mixed solution was put into a hydrothermal reactor (100 mL). The autoclave was put into a preheated oven at 100°C for 24 h and then cooled to room temperature. The precipitate was washed with ethanol and ultra-pure water for several times to get $\beta\text{-Co}(\text{OH})_2$, which was dried at 60°C for 12 h.

2.3. Materials characterization

X-ray diffraction (XRD) pattern was obtained on D/max-2400 diffractometer (Japan Rigaku Rotaflex) with $\text{Cu K}\alpha$ radiation ($\lambda = 154.1 \text{ \AA}$) to obtain the crystal structure. The morphology of as-prepared catalysts was studied by field emission scanning electron microscopy (FESEM, Nova NanoSEM 450). The lattice fringe and microstructure of the materials were characterized by transmission electron microscopy (TEM, FEI TF 30) and the elemental mapping of the products was clarified by energy-dispersive X-ray spectroscopy (EDX, FEI TF 30). The element composition and states of the materials were performed by X-

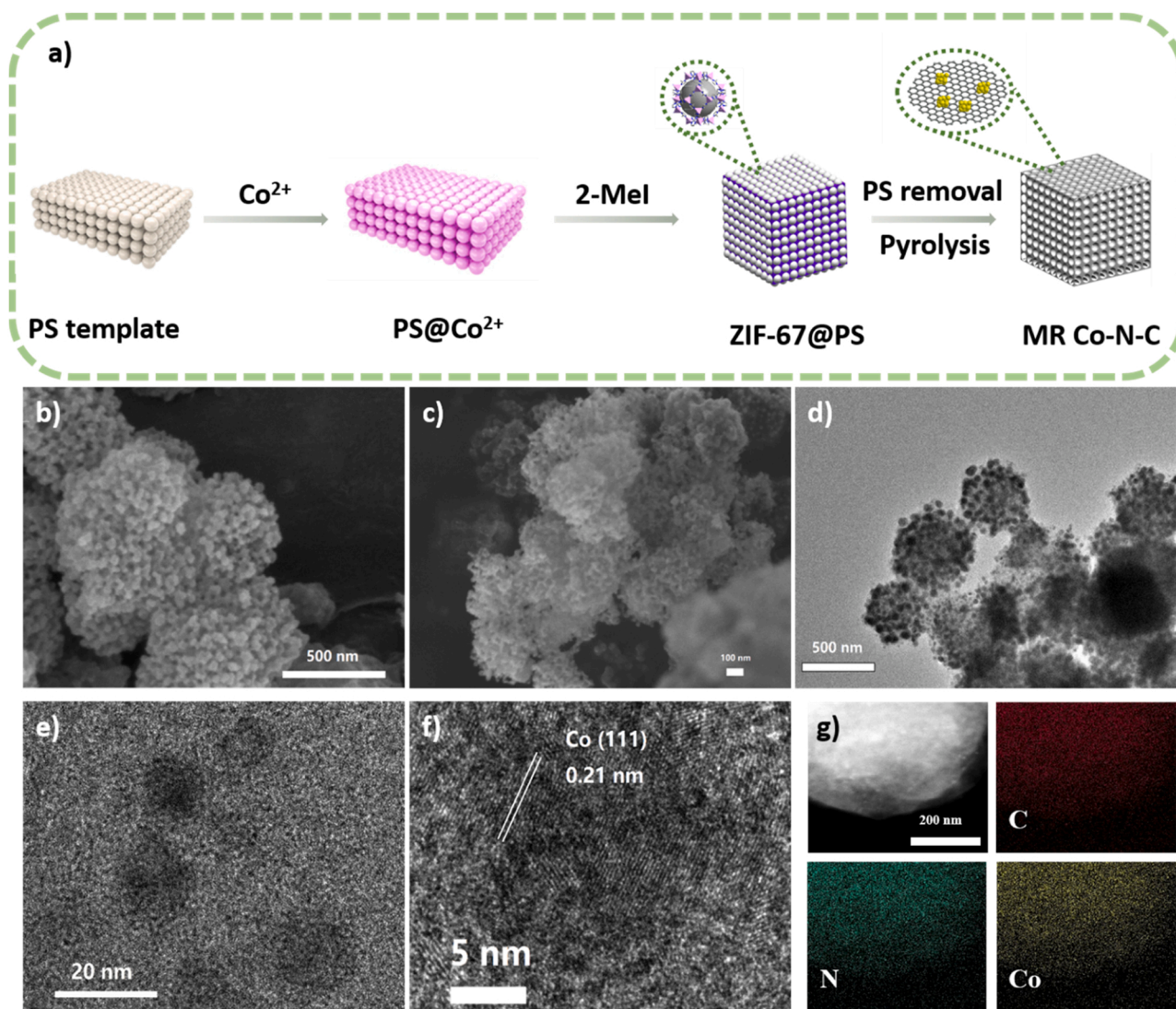


Fig. 1. a) Schematic illustration of the synthesis process of MR Co-NC. b) and c) SEM, d) and e) TEM, and f) HRTEM images of MR Co-NC. g) HAADF-STEM image and the corresponding EDX elemental mappings of MR Co-NC.

ray photoelectron spectroscopy (XPS) (Thermo Scientific ESCALAB 250). Specially, the binding energy was standardized concerning the C 1 s peak at 284.6 eV. Raman spectroscopy was acquired on a DXR Smart using Ar⁺ laser excitation. ¹H NMR spectra were collected at 298 K using Bruker DRX-600 NMR. UV-Vis absorption spectra were recorded on a UV-Vis spectrophotometer (Shimadzu, UV-1800).

More details about the electrochemical measurements, production quantification and computational methods are provided in the supplementary material.

3. Results and discussion

3.1. Synthesis and characterization of catalysts

Fig. 1a illustrates the procedure for preparation of MR Co-NC. First, PS with an average diameter of 70–80 nm were synthesized through emulsion polymerization (Fig. S1). After immersing the PS templates in a Co(NO₃)₃ methanol solution, the PS was modified with Co²⁺ ions, which provide abundant nucleation sites for surface modification. The subsequent immersion of PS@Co²⁺ into a methanol solution of 2-methylimidazole (2-MeI) led to the in-situ growth of ZIF-67 in the voids of PS assembly (ZIF-67 @PS). The final MR Co-NC was obtained by pyrolysis of the resulting composite under Ar atmosphere at 600 °C, which

removed the PS templates and left abundant mesoporous channels. Simultaneously, ZIF-67 was decomposed and converted to N-doped carbonous frameworks integrated with uniformly dispersed cobalt nanoparticles. The above processes are in agreement with the thermogravimetric analysis (TGA) of PS and ZIF-67 @PS, which showed weight loss at 400 °C for PS sublimation and 450–550 °C for ZIF carbonization, respectively (Fig. S2). Meanwhile, cobalt decorated N-doped carbon (Co-NC), cobalt nanoparticles (Co NPs) and N-doped carbon (NC) were also prepared for comparison.

The typical scanning electron microscopy (SEM) images of MR Co-NC show an approximate hexahedron morphology with abundant pores (Fig. 1b and c). The mesoporous feature of MR Co-NC makes the entire framework highly 3-D interconnected and rich with continuous channels, which was proposed to facilitate the dispersion of Co sites throughout the skeleton. This porous structure was also characterized by transmission electron microscopy (TEM) (Fig. 1d). For comparison, the SEM and TEM images in Fig. S3 show a rough surface without visible mesopores for templates-free Co-NC. The magnified TEM image reveals uniformly dispersed Co NPs with an average size of 10–12 nm (Fig. 1e). The HRTEM image shows that the Co NPs are embedded in irregular carbon with a lattice spacing of 0.22 nm corresponding to the (111) facet of metallic Co (PDF # 15–0806) (Fig. 1f). The energy-dispersive X-ray spectroscopy (EDX) analysis exhibits the homogenous distribution of

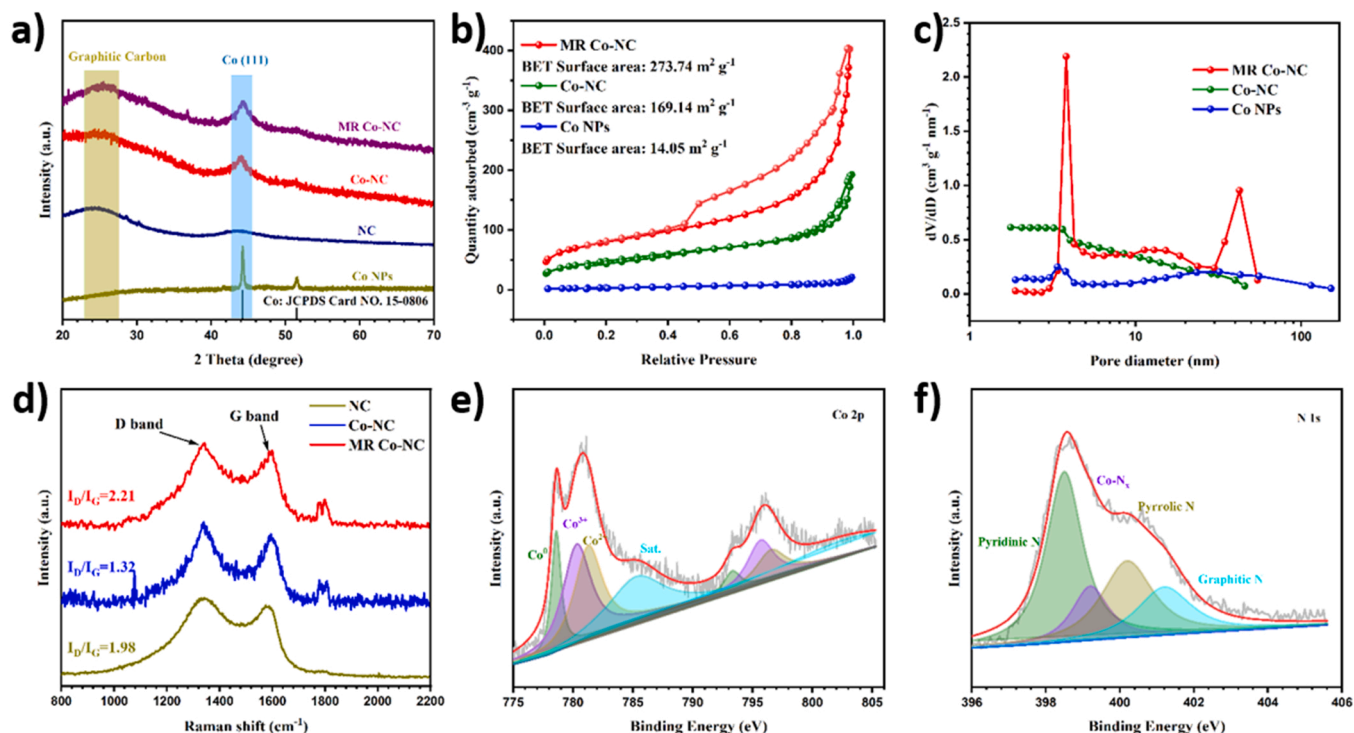


Fig. 2. a) XRD patterns of Co NPs, NC, Co-NC, and MR Co-NC. b) N_2 adsorption-desorption isotherms and c) Pore size distributions of Co NPs, Co-NC, and MR Co-NC. d) Raman spectra of NC, Co-NC, and MR Co-NC. e) Co 2p and e) N 1 s XPS spectra of MR Co-NC.

Co, N, and C elements (Fig. 1g).

The X-ray diffraction (XRD) patterns of both MR Co-NC and Co-NC display the peaks corresponding to graphitic carbon and metallic Co and no other impurities were observed (Fig. 2a), suggesting the successful conversion of ZIF-67 to the Co nanoparticles decorated N-doped carbons by pyrolysis (Fig. S4). The N_2 adsorption-desorption experiments were performed to evaluate the pore structures of the catalysts. A Brunauer-Emmett-Teller (BET) specific area of $273.74 \text{ m}^2 \text{ g}^{-1}$ was obtained for MR Co-NC, which is much larger than those of Co-NC ($169.4 \text{ m}^2 \text{ g}^{-1}$) and Co NPs ($14.05 \text{ m}^2 \text{ g}^{-1}$) (Fig. 2b), this trend is also in line with the results of electrochemical active surface area (ECSA) (Figs. S5 and 6). In accordance with the reported ZIF-derived M-NC composites, the pore size distribution analysis in Fig. 2c reveals a pore size of 3.63 nm for ZIF-67 derived Co-NC material [22,23]. However, two main types of pore size centered at 3.81 and 42.43 nm arising from ZIF-67 carbonization and PS sublimation, respectively, were found for MR Co-NC, indicating the indispensable role of PS templates in formation of hierarchically mesoporous structures. In addition, the electrochemical impedance spectroscopy (EIS) manifested enhanced electron transfer kinetics upon loading Co NPs on the highly conductive carbonous skeleton (Fig. S7) [24]. MR Co-NC with rich mesopores endows this composite material with rapid interfacial electron transportation and facile accessibility of electroactive sites to the reactants. These factors were expected to improve the activity of the new catalyst toward nitrate reduction.

Raman spectra of MR Co-NC show two characteristic D (1340 cm^{-1}) and G (1594 cm^{-1}) bands, corresponding to the defect carbon and graphitic sp^2 -carbon, respectively (Fig. 2d). The increased I_D/I_G ratio for MR Co-NC compared with that of Co-NC indicates more defects created by the introduction of mesopores in MR Co-NC [25]. The electronic structures and coordination environments of the obtained materials were investigated by X-ray photoelectron spectroscopy (XPS). The survey spectrum of MR Co-NC manifests the co-existence of Co, C, N, and O elements (Fig. S8). The high-resolution Co 2p XPS spectrum exhibits characteristic peaks for metallic Co at 778.6 and 793.4 eV. Besides, the peaks of Co^{3+} (780.4 and 795.7 eV) and Co^{2+} (781.25 and 796.7 eV)

accompanied by two satellite peaks at 785.55 and 802.6 eV arising from Co^{2+} reveal the existence of partial oxidation on the surface of MR Co-NC (Fig. 2e) [26]. The deconvoluted N 1 s XPS spectrum can be fitted with four main peaks at 398.5, 399.2, 400.2, and 401.25 eV, which are assigned to the pyridinic N, Co-N_x , pyrrolic N, and graphitic N, respectively (Fig. 2f) [27]. Finally, the content of Co was quantified to be 16.2 wt% by means of inductively coupled plasma optical emission spectroscopy (ICP-OES).

3.2. Electrocatalytic NO_3RR performance

The eNO_3RR performance of the as-prepared catalyst was assessed using a three-electrode setup in an H-cell separated by Nafion membrane (Fig. S9). The catalyst deposited carbon paper (CP) was used as the working electrode, the Ag/AgCl and Pt mesh were served as reference electrode and counter electrode, respectively. First, the linear sweep voltammetry (LSV) was recorded in 0.1 M KOH with and without the presence of nitrate (0.1 M KNO_3). As shown in Fig. 3a, the enhanced current response and a positive shift of the onset potential in the presence of nitrate suggest that the NO_3^- is effectively reduced by MR Co-NC. The chronoamperometry tests were operated to access NH_3 yield rate and FEs for different catalysts (Fig. S10). The produced NH_3 and other possible water-soluble by-products such as NO_2^- , NH_2OH and N_2H_4 were quantitatively analyzed by both ^1H nuclear magnetic resonance (^1H NMR), ion chromatography (IC) and colorimetric methods (Figs. S11–16) [28], while the gaseous products including N_2 and H_2 arising from the competitive HER were quantified by gas chromatography (Fig. S17). The experimental results showed that the current electrocatalytic system is highly selective for NH_3 production and only small amount of NO_2^- and H_2 were detected (Figs. S18–19). As shown in Figs. 3b and 3c, the FE of NH_3 production and the NH_3 yield rate increase with the negative shift of the applied potential over a range of -0.2 – -0.7 V vs. RHE. A maximum FE of $95.35 \pm 1.75\%$ and an NH_3 yield rate of $1.25 \pm 0.023 \text{ mmol h}^{-1} \text{ cm}^{-2}$ were achieved at -0.7 V , which are higher than those of the most state-of-the-art eNO_3RR electrocatalysts, including noble-metal based catalysts such as Pd-TiO₂ [29],

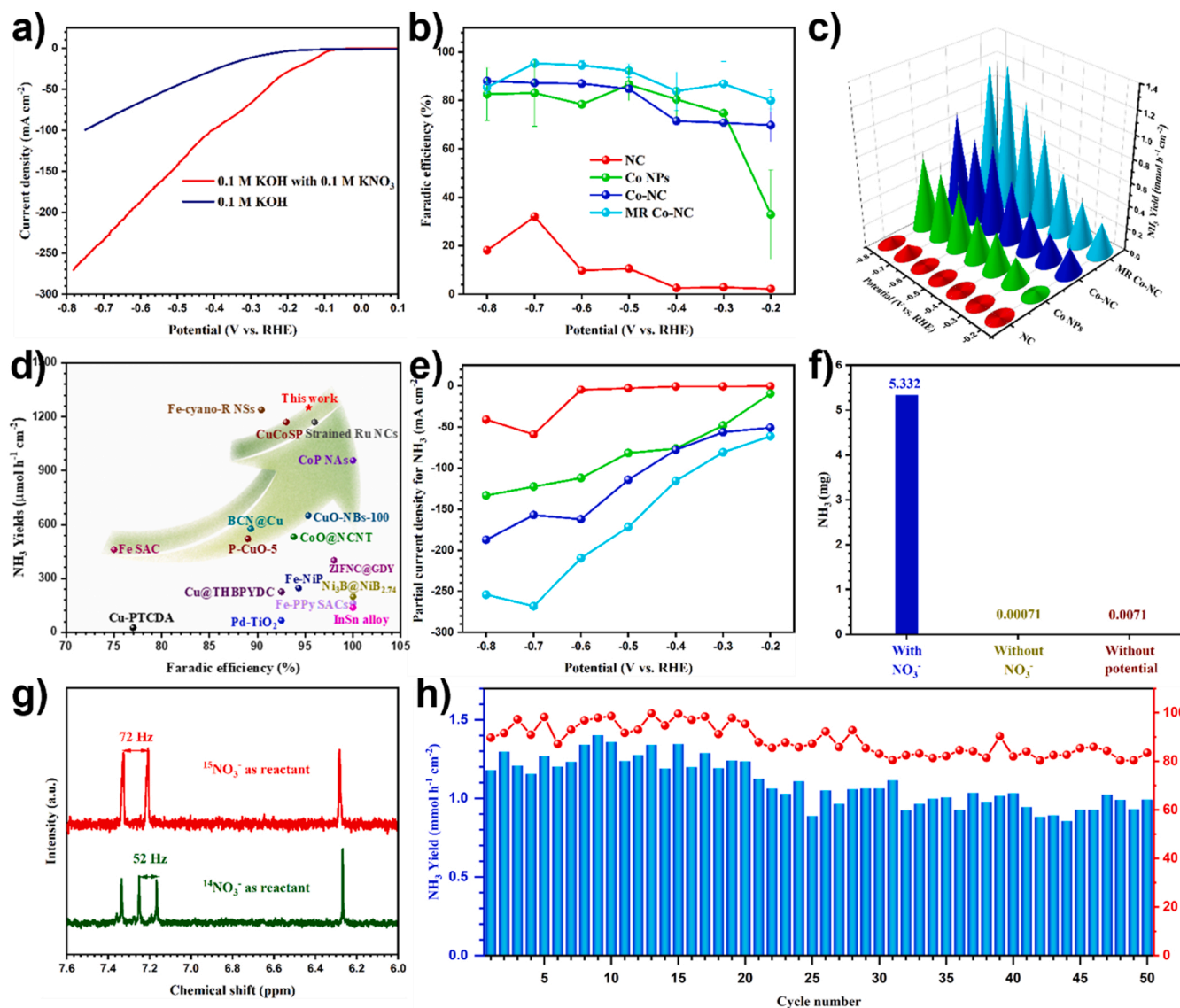


Fig. 3. a) Linear sweep voltammetry of MR Co-NC in 0.1 M KOH with and without the presence of KNO_3 . b) FEs and c) Yield for Co NPs, NC, Co-NC, and MR Co-NC under the potential range of -0.2 – -0.8 V vs. RHE. d) FE values and NH_3 yields of MR Co-NC compared with other recently reported catalysts. e) Partial current densities of ammonia for Co NPs, NC, Co-NC, and MR Co-NC under the potential range of -0.2 – -0.8 V vs. RHE. f) The NH_3 yield of electrolysis over MR Co-NC in 0.1 M KOH electrolyte with KNO_3 at -0.7 V, without KNO_3 at -0.7 V, and without applied potential in the presence of KNO_3 . g) 1H NMR spectra of $^{14}\text{NH}_4^+$ and $^{15}\text{NH}_4^+$ catalyzed by MR Co-NC using K^{14}NO_3 and K^{15}NO_3 as the isotopic sources. h) Cycling tests of MR Co-NC for eNO_3RR at -0.7 V.

Ru@Cu-0.6\% [30], OD-Ag [31], a-RuO_2 [32], $\text{Ru}_1\text{-TiO}_x/\text{Ti}$ [33] and non-noble-metal based catalysts such as Fe SAC [34], $\text{Ni}_3\text{B@NiB}_{2.74}$ [35], $\text{Ni}_1\text{Cu SAA}$ [36], $\text{TiO}_2\text{ NTs/CuO}_x$ [37]. Based on the loading of MR Co-NC (0.6 mg cm^{-2} , Fig. S20), the NH_3 -evolving rate could also be calculated as $2.08 \pm 0.038\text{ mol h}^{-1}\text{ g}_{\text{cat}}^{-1}$, more than 10-fold increase in that of the Haber-Bosch process (Fig. 3d and Table S1). The slight deterioration in FE and yield rate at more negative potential could be attributed to the competitive HER and limited NO_3^- mass transfer. To further demonstrate the advantage of MR Co-NC in nitrate reduction, the performance of Co-NC, Co NPs, and NC toward eNO_3RR were evaluated under identical conditions. It was found that the presence of 3-D mesoporous channels in the carbon skeleton is crucial for efficient NH_3 synthesis as the channel-free Co-NC resulted in almost half reduction in NH_3 yields (Figs. 3b, 3c, S21, and S22). The pore size distribution played a significant role in ammonia synthesis. Among the synthesized materials, MR Co-NC templated by PS diameters of 70–80 nm exhibited the highest activity (Fig. S23). Similarly, the Co NPs achieved a reduced yield rate of $0.57 \pm 0.094\text{ mmol h}^{-1}\text{ cm}^{-2}$ and a lower FE of 83.03

$\pm 13.70\%$ at -0.7 V, which were ascribed to the more pronounced HER process (Figs. S24–25). The metal-free sample of NC also showed significantly reduced eNO_3RR performance with an ammonia yield rate of $93.98 \pm 0.38\text{ }\mu\text{mol h}^{-1}\text{ cm}^{-2}$ and a FE of $32.02 \pm 0.13\%$ at -0.7 V, implying the indispensable role of the Co metal sites in nitrate reduction (Figs. S26–27). In line with these results, MR Co-NC delivers a partial current density of 268 mA cm^{-2} for NH_3 synthesis, which is much higher than the values exhibited by Co-NC and Co NPs (Fig. 3e).

To exclude the inference of external pollution, blank comparisons and isotope labeling experiments were conducted. A negligible amount of NH_3 was detected under open-circuit conditions in the presence of NO_3^- (Fig. 3f). Likewise, no ammonia production was detected without the presence of NO_3^- under short-circuit test conditions. In addition, the nuclear magnetic peak of $^{15}\text{NH}_4^+$ displays as a doublet signal when $^{15}\text{NO}_3^-$ was used as a feeding nitrogen source, and a triplet peak for $^{14}\text{NH}_4^+$ appears in the case of $^{14}\text{NO}_3^-$ as the nitrogen source (Fig. 3g) [38–40]. These findings collectively proved that NO_3^- was the sole source of NH_3 instead of external pollution. To ensure the accuracy of the above test

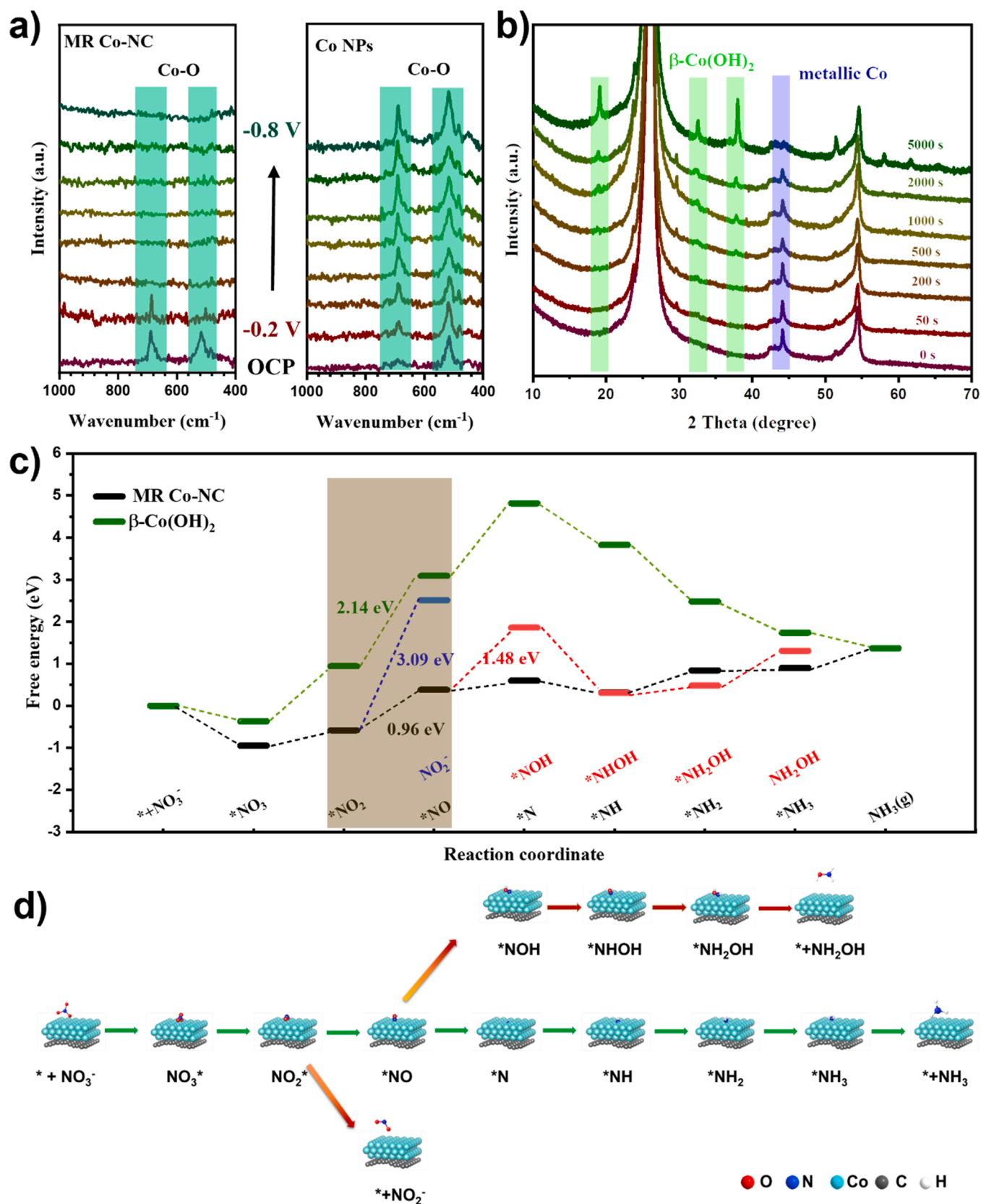


Fig. 4. a) Electrochemical in-situ Raman spectroscopy of MR Co-NC and Co NPs with different potentials in 0.1 M KOH with 0.1 M KNO₃. b) The ex-situ XRD patterns of Co NPs loading on a carbon paper after electrochemical tests for a certain period of time. c) Gibbs free energy diagram of various intermediates generated during eNO₃RR over MR Co-NC and β -Co(OH)₂. d) The proposed reaction pathways for the production of NH₃, NH₂OH and NO₂⁻. The minimum energy pathway is shown in green arrows.

results, the produced ammonia was also quantified by ion chromatography (IC) and ^1H NMR with maleic acid as an external standard. The IC and ^1H NMR results shown in Fig. S28c match well with those obtained by the indophenol method, confirming the reliability of our data. The stability of MR Co-NC in catalysis was investigated by consecutive cycling tests and long-term test at -0.7 V. As depicted in Fig. 3 h, the NH_3 yields and FEs were kept stable for MR Co-NC during 50 cycles of eNO_3RR . A 10 h electrochemical stability test shows a negligible attenuation in current density (Fig. S29). In addition, the morphology and electronic structure of the catalyst were well maintained based on the XPS, TEM, TEM, and XRD measurements before and after the stability test (Figs. S30–31). In comparison, an obvious decrease in NH_3 yield was found by Co NPs during the cycling tests (Fig. S32), implying a beneficial role of the carbon framework on catalyst stability.

3.3. Mechanism investigation of eNO_3RR

To gain insight into the catalytic active species, in-situ Raman spectroscopy was employed to study the structural and chemical change of Co sites during the eNO_3RR . Under open-circuit conditions, the Raman spectra of MR Co-NC and Co NPs show two characteristic peaks of Co-O at 674 and 497 cm^{-1} (Fig. 4a) [41], which agrees well with the XPS analysis that the Co species on the catalyst's surface is partially oxidized in air. When a potential of -0.2 V was applied, the Co-O peaks for MR Co-NC gradually disappear at more negative potentials, consistent with the transformation of CoO_x to metallic Co. In contrast to this observation, the Co-O peaks were found to gradually increase for Co NPs when the potentials decrease from -0.2 to -0.8 V (Fig. 4b). Next, *ex-situ* XRD tests were carried out to monitor the change in the XRD pattern of the Co NP-based electrode at -0.7 V. In a duration of 5000 s, the characteristic X-ray diffraction peak at 44.2° indexed to the (111) crystal plane of metallic Co (PDF# 15-0806) was found to gradually decline accompanied by the appearance of a set of new peaks at 18.8° , 32.2° and 37.65° assigned to the (001), (100), and (101) facets of $\beta\text{-Co}(\text{OH})_2$ (PDF# 03-0443) (Fig. S33). Unfortunately, the signals for metallic Co were fully sheltered owing to the low content of Co and the increased signal intensity of carbon paper. From the enlarged images, the patterns for $\beta\text{-Co}(\text{OH})_2$ were also indiscoverable (Fig. S34). This analysis is in accord with the results from Raman spectroscopy, affirming that the pure Co NPs could be spontaneously reconstructed to $\beta\text{-Co}(\text{OH})_2$ in the process of eNO_3RR under alkaline conditions. By contrast, the carbon-encapsulated Co NPs maintain its Co^0 state owing to the formation of few graphene layers around metallic cores, their close distance to the Co cores results in an increase in their local work function in a way that has stabilized metallic Co against oxidizing to $\text{Co}(\text{OH})_2$ during the process of nitrate reduction reaction. [42].

To shed light on the reaction mechanism and further rationalize the outstanding eNO_3RR activity of MR Co-NC, density functional theory (DFT) calculations were performed. Briefly, nitrate is firstly adsorbed in the Co site to form $^*\text{NO}_3$, the O-N bonds are then cleaved step-by-step to produce $^*\text{NO}_2$, $^*\text{NO}$, and $^*\text{N}$. Subsequently, the stepwise hydrogenation of $^*\text{N}$ occurs to form $^*\text{NH}$, $^*\text{NH}_2$, and $^*\text{NH}_3$. Finally, $^*\text{NH}_3$ is desorbed from the metal site to produce NH_3 (Fig. 4). [43] Notably, the Gibbs free energy barrier of the rate-determining step (RDS) is 3.09 eV for the route of NO_2 (desorption of $^*\text{NO}_2$) production, 1.48 eV for the route of NH_2OH (hydrogenation of $^*\text{NO}$) production and 0.96 eV for NH_3 production (deoxygenation of $^*\text{NO}_2$), respectively. The low free energy barrier was proposed to be the main reason for the excellent NH_3 selectivity exhibited by MR Co-NC via an eight-electron and nine-proton process (Fig. 4d) [44,45]. The Gibbs free energy diagrams in Fig. 4c also reveal that the endothermic deoxygenation of $^*\text{NO}_2$ to form $^*\text{NO}$ is the RDS for both MR Co-NC and $\beta\text{-Co}(\text{OH})_2$ in NH_3 synthesis. However, $\beta\text{-Co}(\text{OH})_2$ shows an uphill free energy change of 2.14 eV, which is markedly higher than that of MR Co-NC (0.96 eV), indicating dramatically suppressed eNO_3RR activity due to the reconstruction of metallic Co [30,46]. These analyses are in good agreement with the experimental results in

Fig. S35, where $\beta\text{-Co}(\text{OH})_2$ displays poor eNO_3RR activity.

4. Conclusions

In summary, we have presented a facile strategy to fabricate a mesopore-rich Co-NC electrocatalyst based on ZIF-derived hybrid structure with PS as the sacrificial template. By taking advantage of the large specific surface area, efficient interfacial electron transfer kinetics, and high intrinsic activity of Co^0 sites, the MR Co-NC delivers an industrial-relevant current density of 268 mA cm^{-2} for eNO_3RR with a maximum FE of $95.35 \pm 1.75\%$ and an NH_3 yield rate up to $1.25 \pm 0.023\text{ mmol h}^{-1}\text{ cm}^{-2}$. The abundant hierarchical mesopores with irregularly interconnected channels and large surface area jointly expedite mass transport, endowing the catalyst with fast reaction kinetics. Besides, the conductive carbon matrix plays a positive effect on preventing the active sites from reconstruction in alkaline solution. Mechanistic studies reveal that Co^0 in MR Co-NC displays a lower free-energy change for the formation of $^*\text{NO}$ in comparison with $\beta\text{-Co}(\text{OH})_2$ derived from the carbon-free Co NPs. This work provides a new horizon for designing highly efficient eNO_3RR catalysts, and it may also be effective for other electrocatalytic reactions.

CRedit authorship contribution statement

Suxian Xu: Methodology, Writing – original draft, Formal analysis, Data curation. **Yongbin Shi:** Validation, Formal analysis. **Zhibing Wen:** Formal analysis, Visualization. **Xiao Liu:** Resources, Data curation. **Yong Zhu:** Methodology, Resources. **Guoquan Liu:** Investigation, Software. **Hua Gao:** Investigation, Resources. **Licheng Sun:** Funding acquisition, Writing – review & editing. **Fei Li:** Conceptualization, Funding acquisition, Writing – review & editing.

Declaration of Competing Interest

The authors declare that they have no competing financial interests or personal relationships that could have appeared to influence the work reported in this paper.

Data Availability

I have shared the link to my data at the attached file step.

Acknowledgements

This work was supported by the National Key R&D Program of China (2022YFA0911904), the National Natural Science Foundation of China (21872016, 22088102, and 22172018), the Fundamental Research Funds for the Central Universities (DUT22QN213) and K&A Wallenberg Foundation.

Appendix A. Supporting information

Supplementary data associated with this article can be found in the online version at doi:10.1016/j.apcatb.2022.122192.

References

- [1] V. Smil, Detonator of the population explosion, 415–415, *Nature* 400 (1999), <https://doi.org/10.1038/22672>.
- [2] J.G. Chen, R.M. Crooks, L.C. Seefeldt, K.L. Bren, R.M. Bullock, M.Y. Danrensbourg, P.L. Holland, B. Hoffman, M.J. Janik, A.K. Jones, M.G. Kanatzidis, P. King, K. M. Lancaster, S.V. Lymar, P. Pfomr, W.F. Schneider, R.R.S. Chrock, Beyond fossil fuel-driven nitrogen transformations, *Science* 360 (2018), eaar6611, <https://doi.org/10.1126/science.aar6611>.
- [3] N. Gilbert, African agriculture: Dirt poor, *Nature* 483 (2012) 525–527, <https://doi.org/10.1038/483525a>.
- [4] D. Chen, L.H. Zhang, J. Du, H. Wang, J. Guo, J. Zhan, F. Li, F. Yu, A tandem strategy for enhancing electrochemical CO_2 reduction activity of single-atom Cu-

- SiN₃ catalysts via integration with Cu nanoclusters, *Angew. Chem. Int. Ed.* 60 (2021) 24022–24027, <https://doi.org/10.1002/anie.202109579>.
- [5] Y. Sun, Y. Han, X. Zhang, W. Cai, Y. Zhang, Z. Li, B. Li, J. Lai, L. Wang, TiO_{1.8} with lattice H for effective electrocatalytic nitrogen fixation, *Appl. Catal. B Environ.* 319 (2022), 121933, <https://doi.org/10.1016/j.apcatb.2022.121933>.
- [6] P. Shen, X. Li, Y. Luo, N. Zhang, X. Zhao, K. Chu, Ultra-efficient N₂ electroreduction achieved over a rhodium single-atom catalyst (Rh₁/MnO₂) in water-in-salt electrolyte, *Appl. Catal. B Environ.* 316 (2022), 121651, <https://doi.org/10.1016/j.apcatb.2022.121651>.
- [7] Z. Xue, S. Zhang, Y. Lin, H. Su, G. Zhai, J. Han, Q. Yu, X. Li, M. Antonietti, J. Chen, Electrochemical reduction of N₂ into NH₃ by donor-acceptor couples of Ni and Au nanoparticles with a 67.8% Faradaic efficiency, *J. Am. Chem. Soc.* 141 (2019) 14976–14980, <https://doi.org/10.1021/jacs.9b07963>.
- [8] L. Han, Z. Ren, P. Ou, H. Cheng, N. Rui, L. Lin, X. Liu, L. Zhuo, J. Song, J. Sun, J. Luo, H.L. Xin, Modulating single-atom palladium sites with copper for enhanced ambient ammonia electrosynthesis, *Angew. Chem. Int. Ed.* 60 (2021) 345–350, <https://doi.org/10.1002/anie.202010159>.
- [9] L. Zhang, M. Cong, X. Ding, Y. Jin, F. Xu, Y. Wang, L. Chen, L. Zhang, A janus Fe-SnO₂ catalyst that enables bifunctional electrochemical nitrogen fixation, *Angew. Chem. Int. Ed.* 59 (2020) 10888–10893, <https://doi.org/10.1002/anie.202003518>.
- [10] P.H. Langevelde, L. Katsounaros, M.T. Koper, Electrocatalytic nitrate reduction for sustainable ammonia production, *Joule* 5 (2021) 290–294, <https://doi.org/10.1016/j.joule.2020.12.025>.
- [11] H. Xu, Y. Ma, J. Chen, W. Zhang, J. Yang, Electrocatalytic reduction of nitrate – a step toward a sustainable nitrogen cycle, *Chem. Soc. Rev.* 51 (2022) 2710–2758, <https://doi.org/10.1039/D1CS00857A>.
- [12] Y. Wang, C. Wang, M. Li, Y. Yu, B. Zhang, Nitrate electroreduction: mechanism insight, in situ characterization, performance evaluation, and challenges, *Chem. Soc. Rev.* 50 (2021) 6720–6733, <https://doi.org/10.1039/D1CS00116G>.
- [13] Y. Zhang, X. Chen, W. Wang, L. Yin, J.C. Crittenden, Electrocatalytic nitrate reduction to ammonia on defective Au₁Cu (111) single-atom alloys, *Appl. Catal. B Environ.* 310 (2022), 121346, <https://doi.org/10.1016/j.apcatb.2022.121346>.
- [14] W.-D. Zhang, H. Dong, L. Zhou, H. Xu, H.-R. Wang, X. Yan, Y. Jiang, J. Zhang, Z.-G. Du, Fe single-atom catalysts with pre-organized coordination structure for efficient electrochemical nitrate reduction to ammonia, *Appl. Catal. B Environ.* 317 (2022), 121750, <https://doi.org/10.1016/j.apcatb.2022.121750>.
- [15] T. Ren, Z. Yu, H. Yu, K. Deng, Z. Wang, X. Li, H. Wang, L. Wang, Y. Xu, Interfacial polarization in metal-organic framework reconstructed Cu/Pd/CuO_x multi-phase heterostructures for electrocatalytic nitrate reduction to ammonia, *Appl. Catal. B Environ.* 318 (2022), 121805, <https://doi.org/10.1016/j.apcatb.2022.121805>.
- [16] R.V. Jagadeesh, K. Murugesan, A.S. Alshammari, H. Neumann, M.M. Pohl, J. Radnik, M. Beller, MOF-derived cobalt nanoparticles catalyze a general synthesis of amines, *Science* 358 (2017) 326–332, <https://doi.org/10.1126/science.aan6245>.
- [17] X. Wang, Y. Jia, X. Mao, D. Liu, W. He, J. Li, J. Liu, X. Yan, J. Chen, L. Song, A. Du, X. Yao, Edge-rich Fe-N₄ active sites in defective carbon for oxygen reduction catalysis, *Adv. Mater.* 32 (2020) 2000966, <https://doi.org/10.1002/adma.202000966>.
- [18] H. Fei, J. Dong, D. Chen, T. Hu, X. Duan, I. Shakir, Y. Huang, X. Duan, Single atom electrocatalysts supported on graphene or graphene-like carbons, *Chem. Soc. Rev.* 48 (2019) 5207–5241, <https://doi.org/10.1039/C9CS00422J>.
- [19] F. Wang, T. Hou, X. Zhao, W. Yao, R. Fang, K. Shen, Y. Li, Ordered macroporous carbonous frameworks implanted with CdS quantum dots for efficient photocatalytic CO₂ reduction, *Adv. Mater.* 33 (2021) 2102690, <https://doi.org/10.1002/adma.202102690>.
- [20] H. Hong, J. Liu, H. Huang, C.A. Etogo, X. Yang, B. Guan, L. Zhang, Ordered macroporous metal-organic framework single crystal and their derivatives for rechargeable aluminum-ion batteries, *J. Am. Chem. Soc.* 141 (2019) 14764–14771, <https://doi.org/10.1021/jacs.9b06957>.
- [21] W. Yao, J. Chen, Y. Wang, R. Fang, Z. Qin, X. Yang, L. Chen, Y. Li, Nitrogen-doped carbon composites with ordered macropores and hollow walls, *Angew. Chem. Int. Ed.* 60 (2021) 23729–23734, <https://doi.org/10.1002/anie.202108396>.
- [22] F. Li, J. Du, X. Li, J. Shen, Y. Wang, Y. Zhu, L. Sun, Integration of FeOOH and zeolitic imidazolate framework-derived nanoporous carbon as an efficient electrocatalyst for water oxidation, *Adv. Energy Mater.* 8 (2018) 1702598, <https://doi.org/10.1002/aenm.201702598>.
- [23] L. Wen, X. Li, R. Zhang, H. Liang, Q. Zhang, C. Su, Y. Zeng, Oxygen vacancy engineering of MOF-derived Zn-doped Co₃O₄ nanopolyhedrons for enhanced electrochemical nitrogen fixation, *ACS Appl. Mater. Interfaces* 13 (2021) 14181–14188, <https://doi.org/10.1021/acsami.0c22767>.
- [24] Y. Xu, K. Ren, T. Ren, M. Wang, Z. Wang, X. Li, L. Wang, H. Wang, Ultralow-content Pd in-situ incorporation mediated hierarchical defects in corner-etched Cu₂O octahedra for enhanced electrocatalytic nitrate reduction to ammonia, *Appl. Catal. B Environ.* 306 (2022), 121094, <https://doi.org/10.1016/j.apcatb.2022.121094>.
- [25] W. Cheng, P. Yuan, Z. Lv, Y. Guo, Y. Qiao, X. Xue, X. Liu, W. Bai, K. Wang, Q. Xu, J. Zhang, Boosting defective carbon by anchoring well-defined atomically dispersed metal-N₄ sites for ORR, OER, and Zn-air batteries, *Appl. Catal. B Environ.* 260 (2020), 118198, <https://doi.org/10.1016/j.apcatb.2019.118198>.
- [26] H. Wang, Y. Jiao, S. Wang, P. Ye, J. Ning, Y. Zhong, Y. Hu, Accelerating triple transport in zinc-air batteries and water electrolysis by spatially confining Co nanoparticles in breathable honeycomb-like macroporous N-doped carbon, *Small* 17 (2021) 2103517, <https://doi.org/10.1002/smll.202103517>.
- [27] W. Yu, J. Yu, Y. Wang, X. Li, Y. Wang, H. Yuan, X. Zhang, H. Liu, W. Zhou, Electrocatalytic upcycling of nitrate and hydrogen sulfide via a nitrogen-doped carbon nanotubes encapsulated iron carbide electrode, *Appl. Catal. B Environ.* 310 (2022), 121291, <https://doi.org/10.1016/j.apcatb.2022.121291>.
- [28] G.F. Chen, Y. Yuan, H. Jiang, S.Y. Ren, L.X. Ding, L. Ma, T. Wu, J. Lu, H. Wang, Electrochemical reduction of nitrate to ammonia via direct eight-electron transfer using a copper-molecular solid catalyst, *Nat. Energy* 5 (2020) 605–613, <https://doi.org/10.1038/s41560-020-0654-1>.
- [29] Y. Guo, R. Zhang, S. Zhang, Y. Zhao, Q. Yang, Z. Huang, B. Dong, C. Zhi, Pd doping-weakened intermediate adsorption to promote electrocatalytic nitrate reduction on TiO₂ nanoarrays for ammonia production and energy supply with zinc-nitrate batteries, *Energy Environ. Sci.* 14 (2021) 3938–3944, <https://doi.org/10.1039/D1EE00806D>.
- [30] H. Liu, X. Lang, C. Zhu, J. Timoshenko, M. Rüscher, L. Bai, N. Guijarro, H. Yin, Y. Peng, J. Li, Z. Liu, W. Wang, B.R. Cuenya, J. Luo, Efficient electrochemical nitrate reduction to ammonia with copper-supported rhodium cluster and single-atom catalysts, *Angew. Chem. Int. Ed.* 61 (2022), e202202556, <https://doi.org/10.1002/anie.202202556>.
- [31] H. Liu, J. Park, Y. Chen, Y. Qiu, Y. Chen, K. Srivastava, S. Gu, B.H. Shanks, L. T. Roling, W. Li, Electrocatalytic nitrate reduction on oxide-derived silver with tunable selectivity to nitrite and ammonia, *ACS Catal.* 11 (2021) 8431–8442, <https://doi.org/10.1021/acscatal.1c01525>.
- [32] Y. Wang, H. Li, W. Zhou, X. Zhang, B. Zhang, Y. Yu, Structurally disordered RuO₂ nanosheets with rich oxygen vacancies for enhanced nitrate electroreduction to ammonia, *Angew. Chem. Int. Ed.* 61 (2022), e202202604, <https://doi.org/10.1002/anie.202202604>.
- [33] Y. Yao, L. Zhao, J. Dai, J. Wang, C. Fang, G. Zhan, Q. Zheng, W. Hou, L. Zhang, Single atom Ru monolithic electrode for efficient chlorine evolution and nitrate reduction, *Angew. Chem. Int. Ed.* 61 (2022), e202208215, <https://doi.org/10.1002/anie.202208215>.
- [34] Z.-Y. Wu, M. Karamad, X. Yong, Q. Huang, D.A. Cullen, P. Zhu, C. Xia, Q. Xiao, M. Shakouri, F.-Y. Chen, J.Y. Kim, Y. Xia, K. Heck, Y. Hu, M.S. Wong, Q. Li, L. Gates, S. Siahrostami, H. Wang, Electrochemical ammonia synthesis via nitrate reduction on Fe single atom catalyst, *Nat. Commun.* 12 (2021) 2870–2879, <https://doi.org/10.1038/s41467-021-23115-x>.
- [35] L. Li, C. Tang, X. Cui, Y. Zheng, X. Wang, H. Hu, S. Zhang, T. Shao, K. Davey, S.-Z. Qiao, Efficient nitrogen fixation to ammonia through integration of plasma oxidation with electrocatalytic reduction, *Angew. Chem. Int. Ed.* 60 (2021) 14131–14137, <https://doi.org/10.1002/anie.202104394>.
- [36] J. Cai, Y. Wei, A. Cao, J. Huang, Z. Jiang, S. Lu, S.-Q. Zang, Electrocatalytic nitrate-to-ammonia conversion with ~100% Faradaic efficiency via single-atom alloying, *Appl. Catal. B Environ.* 316 (2022), 121683, <https://doi.org/10.1016/j.apcatb.2022.121683>.
- [37] W. Qiu, X. Chen, Y. Liu, D. Xiao, P. Wang, R. Li, K. Liu, Z. Jin, P. Li, Confining intermediates within a catalytic nanoreactor facilitates nitrate-to-ammonia electrosynthesis, *Appl. Catal. B Environ.* 315 (2022), 121548, <https://doi.org/10.1016/j.apcatb.2022.121548>.
- [38] Y. Zhao, F. Li, W. Li, Y. Li, C. Liu, Z. Zhao, Y. Shan, Y. Ji, L. Sun, Identification of M-NH₂-NH₂ intermediate and rate determining step for nitrogen reduction with bioinspired sulfur-bonded FeW catalyst, *Angew. Chem. Int. Ed.* 60 (2021) 20331–20341, <https://doi.org/10.1002/anie.202104918>.
- [39] Y. Li, J. Li, J. Huang, J. Chen, Y. Kong, B. Yang, Z. Li, L. Lei, G. Chai, Z. Wen, L. Dai, Y. Hou, Mn–O covalency governs the intrinsic activity of Co-Mn spinel oxides for boosted peroxymonosulfate activation, *Angew. Chem. Int. Ed.* 60 (2021) 2–10, <https://doi.org/10.1002/anie.202010828>.
- [40] Y. Xu, Y. Wen, T. Ren, H. Yu, K. Deng, Z. Wang, X. Li, L. Wang, H. Wang, Engineering the surface chemical microenvironment over CuO nanowire arrays by polyaniline modification for efficient ammonia electrosynthesis from nitrate, *Appl. Catal. B Environ.* 320 (2023), 121981, <https://doi.org/10.1016/j.apcatb.2022.121981>.
- [41] A.V. Ravindra, B.C. Behera, P. Padhan, O.I. Lebedev, W. Prellier, Tailoring of crystal phase and Néel temperature of cobalt monoxides nanocrystals with synthetic approach conditions, *J. Appl. Phys.* 116 (2014), 033912, <https://doi.org/10.1063/1.4890512>.
- [42] H. Khani, N.S. David, D.O. Wipf, J.B. Goodenough, Graphitic-shell encapsulation of metal electrocatalysts for oxygen evolution, oxygen reduction, and hydrogen evolution in alkaline solution, *Adv. Energy Mater.* 10 (2019) 1903215, <https://doi.org/10.1002/aenm.201903215>.
- [43] A. Kumar, J. Lee, M.G. Kim, B. Debnath, X. Liu, Y. Hwang, Y. Wang, X. Shao, A. R. Jadhav, Y. Liu, H. Tuysuz, H. Lee, Efficient nitrate conversion to ammonia on f-block single-atom/metal oxide heterostructure via local electron-deficiency modulation, *ACS Nano* 16 (2022) 15297–15309, <https://doi.org/10.1021/acsnano.2c06747>.
- [44] O.Q. Carvalho, R. Marks, H.K.K. Nguyen, M.E.V. Sullivan, S.C. Martinez, L. Arnadottir, K.A. Stoerzinger, Role of electronic structure on nitrate reduction to ammonium: a periodic journey, *J. Am. Chem. Soc.* 144 (2022) 14809–14818, <https://doi.org/10.1021/jacs.2c05673>.
- [45] Z.L. Xie, D. Wang, X.Q. Gong, Theoretical insights into nitrate reduction to ammonia over Pt/TiO₂: Reaction mechanism, activity regulation, and catalyst design, *ACS Catal.* 12 (2022) 9887–9896, <https://doi.org/10.1021/acscatal.2c01694>.
- [46] J. Zhou, F. Pan, Q. Yao, Y. Zhu, H. Ma, J. Niu, J. Xie, Achieving efficient and stable electrochemical nitrate removal by in-situ reconstruction of Cu₂O/Cu electroactive nanocatalysts on Cu foam, *Appl. Catal. B Environ.* 317 (2022), 121811, <https://doi.org/10.1016/j.apcatb.2022.121811>.